AGU Advances

Supporting Information for

Upscaling wetland methane emissions from the FLUXNET-CH4 eddy covariance network (UpCH4 v1.0): Model development, network assessment, and budget comparison

Authors and Affiliations

1. **Gavin McNicol***
    a. Department of Earth System Science, Stanford University, Stanford, California, USA
    b. Department of Earth and Environmental Sciences, University of Illinois Chicago, Chicago, Illinois, USA
2. **Etienne Fluet-Chouinard**
    a. Department of Earth System Science, Stanford University, Stanford, California, USA
    b. Institute for Atmospheric and Climate Science, Department of Environmental Systems Science, ETH Zurich, 8092 Zurich, Switzerland
3. **Zutao Ouyang**
    a. Department of Earth System Science, Stanford University, Stanford, California, USA
4. **Sara Knox**
    a. Department of Geography, The University of British Columbia, Vancouver, British Columbia, Canada
5. **Zhen Zhang**
    a. Department of Geographical Sciences, University of Maryland, College Park, Maryland, USA
6. **Tuula Aalto**
    a. Finnish Meteorological Institute, Climate Change, Helsinki, Finland
7. **Sheel Bansal**
    a. U.S. Geological Survey, Northern Prairie Wildlife Research Center, Jamestown, North Dakota, USA
8. **Kuang-Yu Chang**
    a. Earth and Environmental Sciences Area, Lawrence Berkeley National Laboratory, Berkeley, California, USA
9. **Min Chen**
    a. Department of Forest and Wildlife Ecology, University of Wisconsin-Madison, Wisconsin, USA
10. **Kyle Delwiche**

a. Department of Environmental Science, Policy, and Management, University of California, Berkeley, California, USA

11. **Sarah Feron**
    a. Knowledge Infrastructure, University of Groningen, Groningen, Netherlands
12. **Mathias Goeckede**
    a. Department for Biogeochemical Signals, Max Planck Institute for Biogeochemistry, Jena, Germany
13. **Jinxun Liu**
    a. U.S. Geological Survey, Western Geographic Science Center, Moffett Field, California, USA
14. **Avni Malhotra**
    a. Department of Geography, University of Zurich, Zurich, Switzerland
15. **Joe R. Melton**
    a. Climate Research Division, Environment and Climate Change Canada, Victoria, British Columbia, Canada
16. **William Riley**
    a. Earth and Environmental Sciences Area, Lawrence Berkeley National Laboratory, Berkeley, California, USA
17. **Rodrigo Vargas**
    a. Department of Plant and Soil Sciences, University of Delaware, Newark, Delaware, USA
18. **Kunxiaojia Yuan**
    a. Earth and Environmental Sciences Area, Lawrence Berkeley National Laboratory, Berkeley, California, USA
19. **Qing Ying**
    a. Earth System Science Interdisciplinary Center, University of Maryland, College Park, Maryland, USA
20. **Qing Zhu**
    a. Earth and Environmental Sciences Area, Lawrence Berkeley National Laboratory, Berkeley, California, USA
21. **Pavel Alekseychik**
    a. Natural Resources Institute Finland (LUKE), Helsinki, Finland
22. **Mika Aurela**
    a. Finnish Meteorological Institute, PO Box 501, 00101 Helsinki, Finland
23. **David P. Billesbach**
    a. University of Nebraska-Lincoln, Department of Biological Systems Engineering, Lincoln, NE 68583, USA
24. **David I. Campbell**
    a. School of Science, University of Waikato, Hamilton, New Zealand
25. **Jiquan Chen**
    a. Center for Global Change and Earth Observations, Michigan State University, East Lansing, MI 48823
26. **Housen Chu**

a. Climate and Ecosystem Sciences Division, Lawrence Berkeley National Lab, Berkeley, CA 94702, USA

27. **Ankur R. Desai**
    a. Dept. of Atmospheric and Oceanic Sciences, University of Wisconsin-Madison, Madison, WI 53706 USA
28. **Eugenie Euskirchen**
    a. University of Alaska Fairbanks, Institute of Arctic Biology, Fairbanks, AK, USA 99775
29. **Jordan Goodrich**
    a. School of Science, University of Waikato, Hamilton, New Zealand
30. **Timothy Griffis**
    a. Dept. Soil, Water, and Climate, University of Minnesota Twin Cities, St. Paul, MN, USA
31. **Manuel Helbig**
    a. Department of Physics and Atmospheric Science, Dalhousie University, Halifax, Nova Scotia, Canada
32. **Takashi Hirano**
    a. Research Faculty of Agriculture, Hokkaido University, Sapporo, Japan
33. **Hiroki Iwata**
    a. Department of Environmental Science, Faculty of Science, Shinshu University
34. **Gerald Jurasinski**
    a. Landcape Ecology, University of Rostock, Rostock, Germany
    b. Peatland Science, University of Greifswald, Greifswald, Germany
35. **John King**
    a. Department of Forestry and Environmental Resources, North Carolina State University, Raleigh, NC, USA
36. **Franziska Koebsch**
    a. Bioclimatology, University of Göttingen, Göttingen, Germany
37. **Randall Kolka**
    a. USDA Forest Service Northern Research Station, Grand Rapids, MN, USA
38. **Ken Krauss**
    a. USGS Wetland and Aquatic Research Center, Lafayette LA, USA
39. **Annalea Lohila**
    a. Finnish Meteorological Institute, PO Box 501, 00101 Helsinki, Finland
    b. Institute for Atmospheric and Earth System Research/Physics, Faculty of Science, University of Helsinki, Helsinki, Finland
40. **Ivan Mammarella**
    a. Institute for Atmospheric and Earth System Research/Physics, Faculty of Science, University of Helsinki, Helsinki, Finland
41. **Mats Nilson**
    a. Dept. of Forest Ecology and Management, Swedish University of Agricultural Sciences, 901 83 Umeå, Sweden
42. **Asko Noormets**

a. Dept. of Ecology and Conservation Biology, Texas A&M University, TX, USA

43. Walter Oechel

a. Dept. Biology, San Diego State University, San Diego, CA 92182, USA

44. Matthias Peichl

a. Dept. of Forest Ecology and Management, Swedish University of Agricultural Sciences, 901 83 Umeå, Sweden

45. Torsten Sachs

a. GFZ German Research Centre for Geosciences, Telegrafenberg, 14473 Potsdam, Germany

46. Ayaka Sakabe

a. Hakubi center, Kyoto University, Kyoto, Japan

47. Christopher Schulze

a. University of Alberta, Renewable Resources; Université de Montréal, Département de géographie, Université de Montréal, Montréal, QC H2V 0B3, Canada

48. Oliver Sonnentag

a. Département de géographie, Université de Montréal, Montréal, Québec, Canada

49. Ryan C. Sullivan

a. Environmental Science Division, Argonne National Laboratory, Lemont, IL, USA

50. Eeva-Stiina Tuittila

a. School of Forest Sciences, University of Eastern Finland, Joesnuu, Finland

51. Masahito Ueyama

a. Graduate School of Agriculture, Osaka Metropolitan University, Sakai, Japan

52. Timo Vesala

a. Institute for Atmospheric and Earth System Research/Physics, Faculty of Science, University of Helsinki, Helsinki, Finland

b. Institute for Atmospheric and Earth System Research/Forest Sciences, Faculty of Agriculture and Forestry, University of Helsinki, Helsinki, Finland

53. Eric Ward

a. USGS Wetland and Aquatic Research Center, Lafayette, LA, USA

54. Christian Wille

a. GFZ German Research Centre for Geosciences, Telegrafenberg, 14473 Potsdam, Germany

55. Guan Xhuan Wong

a. Sarawak Tropical Peat Research Institute, Sarawak, Malaysia

56. Donatella Zona

a. Dept. Biology, San Diego State University, San Diego, CA 92182, USA

b. Department of Animal and Plant Sciences, University of Sheffield, Western Bank, Sheffield, S10 2TN, United Kingdom

57. Lisamarie Windham-Myers

a. U.S. Geological Survey, Water Mission Area, Menlo Park, California, USA

58. **Benjamin Poulter**
    a. Biospheric Sciences Laboratory, NASA Goddard Space Flight Center, Greenbelt, Maryland, USA
59. **Robert B. Jackson**
    a. Department of Earth System Science, Stanford University, Stanford, California, USA
    b. Woods Institute for the Environment, Stanford University, Stanford, California
    c. Precourt Institute for Energy, Stanford University, Stanford, California

Corresponding Authors

Gavin McNicol

Department of Earth System Science, Stanford University, Stanford, California

Now at: Department of Earth and Environmental Sciences, University of Illinois Chicago

845 West Taylor Street, SES 2440, MC 186, Chicago, Illinois 60607

gmcnicol@uic.edu

https://orcid.org/0000-0002-6655-8045

Etienne Fluet-Chouinard

Department of Earth System Science, Stanford University, Stanford, California

Now at: ETH Zurich, Switzerland

efluet@stanford.edu

https://orcid.org/0000-0003-4380-2153

Contents of this file

AGU PUBLICATIONS

Any use of trade, firm, or product names is for descriptive purposes only and does not imply endorsement by the U.S. Government.

Supporting Text

Text S1. Detailed description of candidate predictor data and preprocessing steps.

The climate predictors included nineteen bioclimatic variables representing summary statistics (mean, min, max, range, isothermality, etc.) for decadal temperature and precipitation (WorldClim 2.0; Fick and Hijmans, 2017), MODIS snow cover (Hall and Riggs, 2016) and MODIS nighttime surface temperature (MOD11A2; Wan et al. 2015). Biometeorology predictors included data from 14 tower-measured or-derived variables (air temperature, gross primary production, incoming shortwave radiation, etc.) which were filtered and gap-filled during tower data pre- and post-processing (Knox et al., 2019) and computed as weekly means or sums (precipitation). Flux-tower associated soil temperature and water table depth were only available at 24 sites and thus were not included, however, other proxies for soil moisture were included (see below). Other biometeorological predictors included observed values and the annual range and normalized seasonality for an actual evapotranspiration product (Terraclimate; Abatzoglou et al. 2018) and a global nitrogen and sulfur deposition product for the year 2000 (Lamarque et al., 2013).

Land cover predictors included the annual range and normalized monthly seasonality of the inundated fraction from a microwave-based wetland product (WAD2M) (Zhang et al. 2021); fractional tree, shrub, and bare earth cover (Sexton et al., 2013); global forest canopy height (Simard et al., 2011); and fraction of human agricultural and urban development (EarthEnv Cover; Tuanmu and Jetz, 2014). Greenness predictors included 14 measures of land surface heterogeneity (EarthEnv Habitat Heterogeneity; Tuanmu and Jetz, 2015) and MODIS vegetation indices (MCD15A2H; Myneni et al., 2015; Vermote, 2015). Soil and relief predictors consisted of six static soil properties (SoilGrids250m; Hengl et al., 2017), a monthly soil water product (TerraClimate; Abatzoglou et al., 2018), 11 topographic properties (EarthEnv Topography; Amatulli et al., 2018), and compound topographic index (GeoMorpho90m; Amatulli et al., 2019). The generic predictor was computed

potential radiation at the top of the atmosphere; found to be useful in high latitude CH4 flux upscaling (Peltola et al., 2019).

Remote sensing indices (included in land cover and vegetation greenness classes) including normalized difference vegetation index (NDVI) and enhanced vegetation index (EVI) (Huete et al., 2002), and surface water indices including simple ratio water index (SRWI) (Zarco-Tejada and Ustin, 2001), land surface water index (LSWI) (Xiao et al., 2002), and normalized difference water index (NDWI) (Gao, 1996) were computed from 8-day, 500 m resolution Terra MODIS surface reflectance products (MOD09A1; (Myneni et al., 2015; Vermote, 2015). These indices together can reflect various biophysical conditions that are correlated to canopy coverage, surface and canopy water content, and soil background. Quality control was applied to exclude bad observations under cloudy, high view angle, or high solar zenith angle conditions based on MODIS data quality flags. Additionally, when snow cover is present, values of these indices become meaningless, and are therefore excluded. QC-created short gaps (1 to 2 8-day periods) which were linearly interpolated and long gaps (>3 8-day periods) were filled using the 2000-2018 mean seasonal cycles. Occasionally, in some northern sites where good values of water indices were not available in the winter season due to long-term snow cover, the site 5th percentile values were assigned. MODIS remote sensing data, when computed for training data at the tower locations, were based on time-series surface reflectance/temperature extracted at the 500-m MODIS pixel that overlap with the tower location using the AppEEARS platform (https://lpdaac.usgs.gov/tools/appeears/) provided by the U.S. Geological Survey (USGS) and the National Aeronautics and Space Administration (NASA).

Further information about predictor datasets is provided in Table S3 and a processed training dataset and code used in our model development will be made available via the McNicol Lab Github (https://github.com/McNicol-Lab).

Text S2. Forward feature selection

A preliminary predictor subset was selected at the performance inflection point, where the cost function stopped decreasing. Within each FFS iteration, a random forest model (Breiman, 2001) was trained for each data fold (all-but-one clusters), and validated on the held-out cluster. Predictions were aggregated across all held-out data and were compared to observations to compute the mean absolute error (MAE) as the cost function metric. MAE was chosen, rather than squared error metrics, for its lower sensitivity to outliers and highly skewed data, which are characteristic of CH4 flux data (Morin, 2019). Limited hyperparameter tuning was

performed during FFS iterations and tree depth was kept relatively shallow during FFS (mtry = 2; min.node.size = 50) to reduce computation time and avoid overfitting. All modeling was performed using R (R Core Team 2022) using the 'caret' (Kuhn, 2020) and 'ranger' packages (Wright and Ziegler, 2017).

Text S3. Technical description of two global wetland extent products used in this methane flux upscaling study.

Description of WAD2M wetland extent: The global Wetland Area and Dynamics for Methane Modeling (WAD2M, version 1.0) is a dataset representing surface inundation at a 0.25deg resolution (~25 km at the Equator) at a monthly time step over 2000–2018 (Zhang et al. 2021). WAD2M was generated by combining a time series of surface inundation estimated from active and passive microwave remote sensing (SWAMPS; Schroeder et al. 2015; Jensen and Mcdonald 2019) with six static datasets that discriminate inland waters, agriculture, shoreline, and non-inundated wetlands. Through this data fusion, WAD2M was tailor made to represent exclusively vegetated wetlands, and enable modeling of their methane fluxes without confusion with other aquatic ecosystems. WAD2M was used to scale the methane fluxes predicted by a bottom-up land surface model ensemble in the most recent Global Carbon Project global methane budget (Saunois et al. 2020), making them directly comparable to the WAD2M-scaled emissions from the upscaling in the present analysis.

Description of GIEMS v2 wetland extent: GIEMSv2 represents global inundation across the world (Prigent et al. 2020). We subset the time-series of GIEMSv2 to its overlapping period with WAD2M of 2001-2015. To provide a comparison to the estimates of vegetated wetland from WAD2M, we performed similar correction steps as were done for WAD2M. We supplemented the wetland cover by offsetting the long-term maximum (F_{max}) to match that from static maps. Diverging from the WAD2M methodology, we subtracted the monthly water cover estimated by Pekel et al. (2016) instead of using the static average water cover. Using this dynamic water cover removed the need to use a coastal water mask. The correction of GIEMSv2 lowered the global mean annual maximum inundated area from 8.98 Mkm^2 down to 7.73 Mkm^2 (**Figure S3**).

Text S4. Global dissimilarity analysis description.

Evaluation of the global representativeness of the network data with respect to the multivariate predictor space of the model can provide insight into the likelihood and severity of extrapolation from machine learning training conditions (Villarreal et al. 2018, 2019; Villarreal and Vargas 2021). Moreover, evaluating the extrapolation domain can inform model selection between two or more candidates that perform equally well during cross validation, but that differ in the plausibility of their extrapolations, even when cross validation is designed to avoid overfitting. For example, Behrens et al. (2018) identified unrealistic rectangular patterns in decision tree model predictions when geolocation predictors, such as XY coordinates, are included.

Distances were computed with the 'dist' function in the 'proxy' R package (Meyer and Buchta, 2020). Predictors were first rescaled (to between zero and one), and weighted in proportion to their average unscaled variable importance in the random forest ensemble. We partially accounted for temporal representativeness (Chu et al., 2017) by computing dissimilarity for each month of the MSC. Predictor vectors were extracted for each site-month from gridded data and therefore sometimes differ from the weekly model training data, but are consistent with the global product forcing data. Global dissimilarity was evaluated at each 0.25° pixel with non-zero wetland cover at a monthly time-step. In each evaluation, all site-month vectors were available for distance computations. This method resembles the random forest training conditions whereby the model was trained on all training data at once and means that the closest tower-month for a given pixel may be of a different month. For instance, a pixel in northern Alaska during July could hypothetically be found to be very similar to a tropical site (e.g., BR-Npw) in January and thus would be assigned a low dissimilarity score in spite of the geographic distance and time between these observation sites.

Text S5. Description of unweighted UpCH4 flux products and flux patterns

The intermediate output of the upscaling was a global surface of wetland CH4 flux predictions, produced after forcing the model with globally gridded predictor data, but prior to wetland area weighting. Thus, the spatial pattern of these "potential" wetland CH4 fluxes is interpreted with attention to the fact that wetland extent in many regions could be very small or non-existent, despite the model predicting high fluxes. Nonetheless, the potential flux output can be used to: 1) visualize model behavior during global grid extrapolation using the same scale and units as the

training flux data; and 2) provide further model validation by comparing gridded predictions against training and additional test sites (pixel-to-tower comparisons).

For regions and months with non-zero WAD2M wetland cover, global 2001-2018 predicted wetland CH4 fluxes followed a long-tailed distribution (Figure S8) with a mean of 63.4 nmol m-2 s-1 and median of 42.2 nmol m-2 s-1, interquartile range of 16.3 - 93.5 nmol m-2 s-1, and min-max range of 0.8 - 282.3 nmol m-2 s-1. Regional flux patterns (Figure S8) largely reflected the dominance of air temperature as a model predictor with the highest mean fluxes (> 200 nmol m-2 s-1) predicted for hot and arid or semi-arid tropical or subtropical regions (e.g., the Sahel, Australia, southwestern United States and northern Mexico, and the Arabian peninsula), while cooler temperatures in tropical forested regions (e.g., Amazon and Congo Basins, and southeast Asia) displayed lower fluxes (< 50 nmol m-2 s-1). Tall canopy heights in tropical forests may also have lowered flux predictions in these regions due to the negative model functional relationship between canopy height and CH4 flux (Figure S6).

Supporting Figures

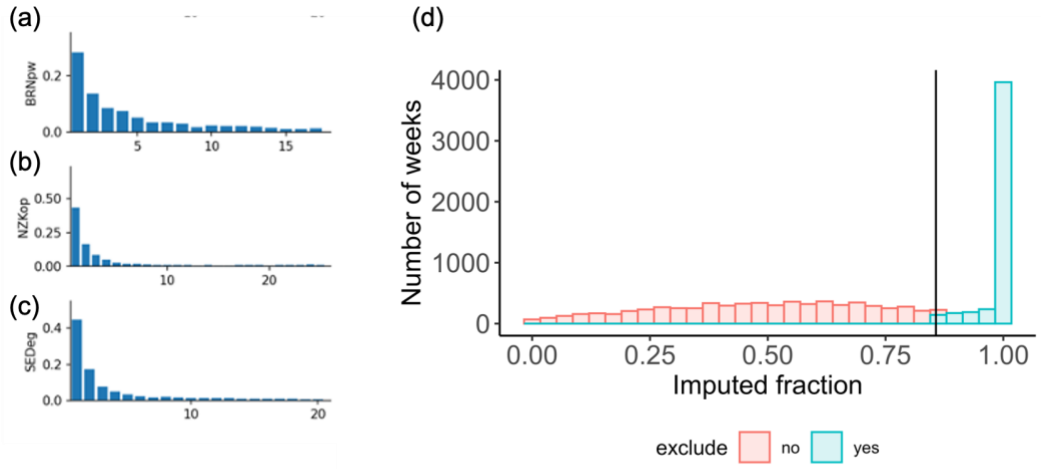

Figure S1. (a-c) (Adapted from Irvin et al. 2021) Examples of gap-length distributions for eddy covariance methane flux data at three distinctive sites (BR-Npw, tropical swamp; NZ-Kop, temperate bog; SE-Deg, boreal fen) included in the FLUXNET-CH4 dataset Version 1.0 and upscaling. The distributions show that the large majority of gaps are very short (1 half-hour) or short (2-8 half-hours), thus, (d) most weekly averaged training data included some gap-filled data, and the imputed fraction was almost evenly distributed from from zero to 0.857 (upper 1-day threshold). A large proportion of the total dataset was excluded which consisted of gaps longer than 1 week.

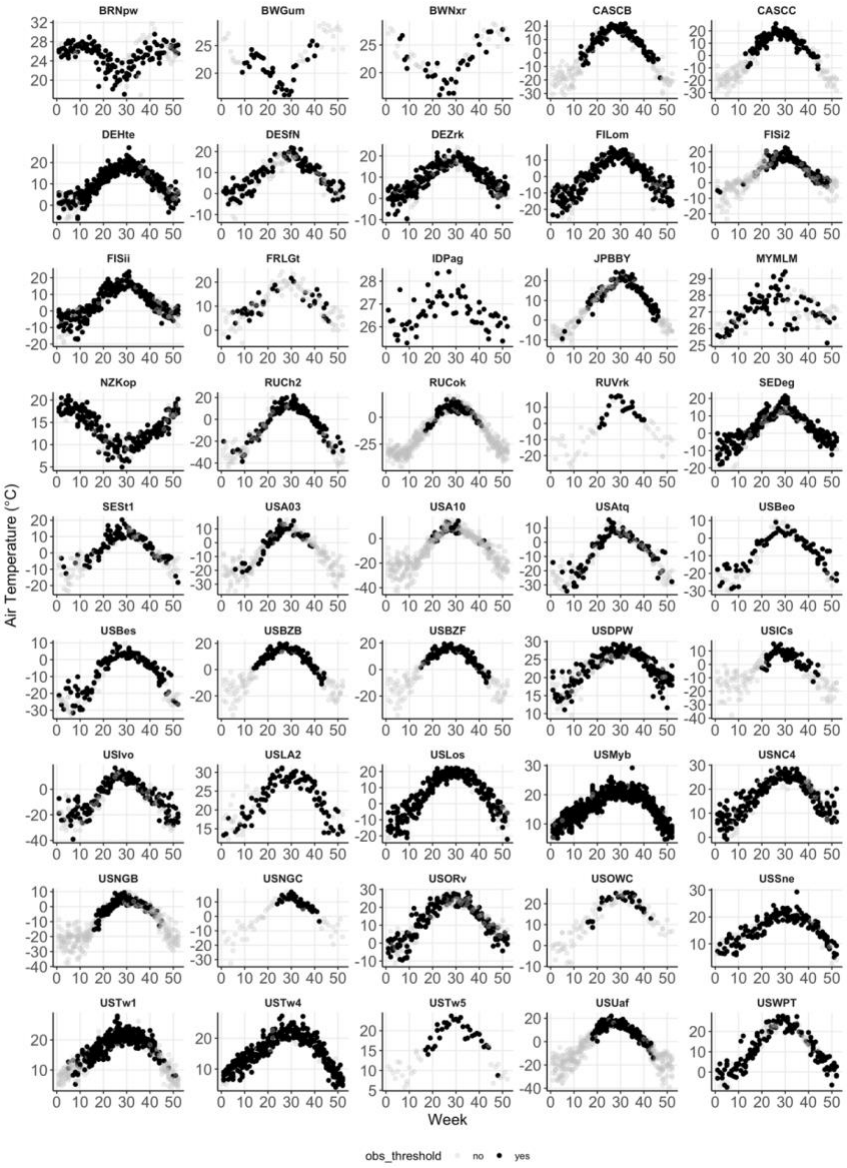

Figure S2. Example of QAQC plots (here, flux tower-measured weekly mean air temperature) generated for each site and candidate predictor combination used to identify and filter outliers or other erroneous data. Grey circles are data excluded by the imputation filter imposed on methane flux values.

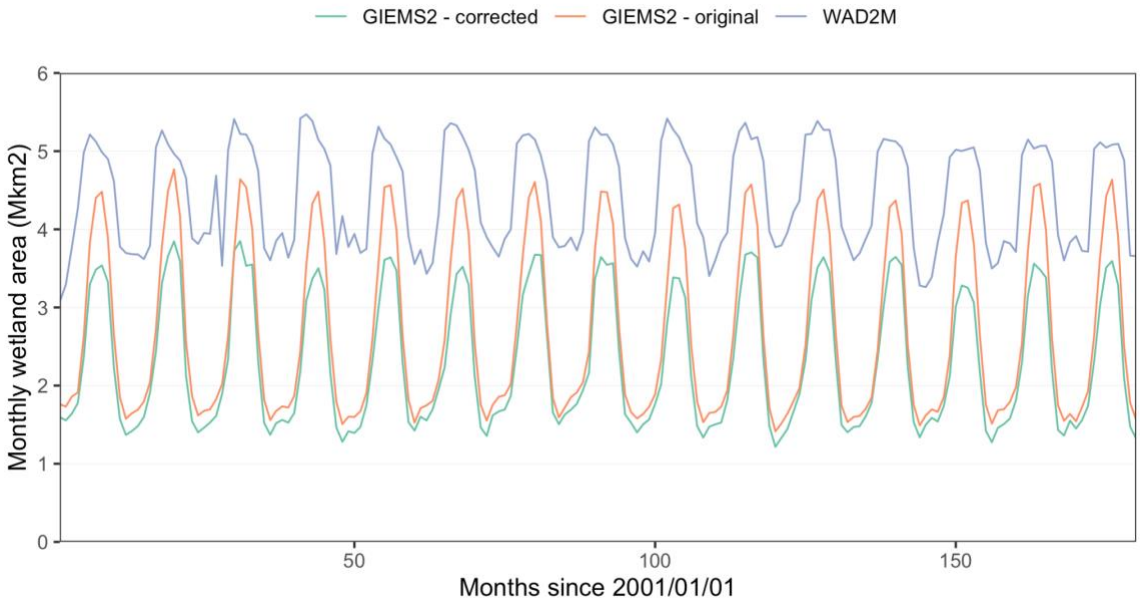

Figure S3. Comparison of monthly wetland area (Mkm^2) for January 2001 to December 2015 according to the two wetland maps used (GIEMSv2 (Prigent et al. 2020) and WAD2M (Zhang et al. 2021)).

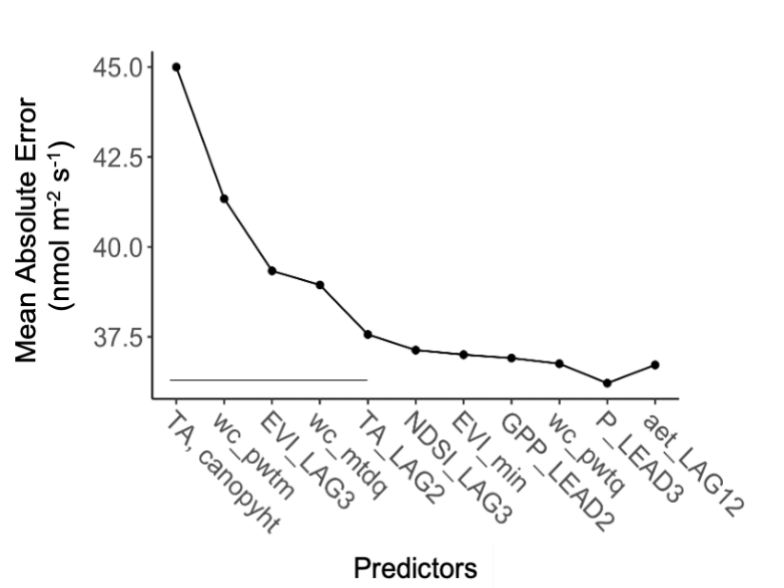

Figure S4. Evolution of model cost function (mean absolute error) during forward feature selection. The best-performing feature pair was added first (far left of x axis) then single additional predictors were added in a stepwise fashion. The horizontal bar length encompasses the 6 final model predictors, after which model performance improvements were marginal. TA = tower-measured air temperature at 2 m; canopy height = global vegetation canopy height; wc_pwtm = WorldClim 2.0 precipitation of the wettest month; EVI_LAG3 = MODIS enhanced vegetation index with a three week lag; wc_mtdq = WorldClim 2.0 mean temperature of the driest quarter; TA_LAG2 = tower-measured air temperature at 2 m with a two week lag; NDSI_LAG3; MODIS normalized difference snow index with a three week lag; EVI_min = MODIS enhanced vegetation index annual minimum value; GPP_LEAD2 = MODIS gross primary production with a two week lead; wc_pwtq = WorldClim 2.0 precipitation of the wettest quarter; P_LEAD3 = tower-measured precipitation with a

three week lead; aet_LAG12 = TerraClimate actual evapotranspiration with a 12 week lag. Predictor abbreviations and data sources are detailed in Table S3.

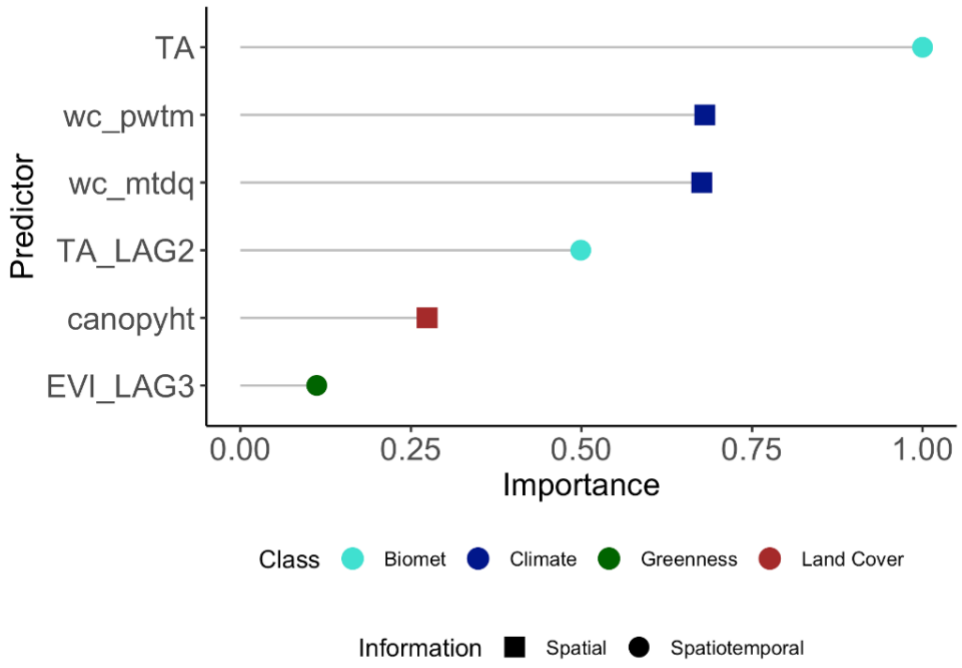

Figure S5. Random forest model predictors ranked using the permutation importance method and rescaled so that importance of the top variable (TA) was equal to 1. TA = tower-measured air temperature at 2 m; canopy height = global vegetation canopy height; wc_pwtm = WorldClim 2.0 precipitation of the wettest month; EVI_LAG3 = MODIS enhanced vegetation index with a three week lag; wc_mtdq = WorldClim 2.0 mean temperature of the driest quarter; TA_LAG2 =

tower-measured air temperature at 2 m with a two week lag; Predictor abbreviations are also detailed in Table S3.

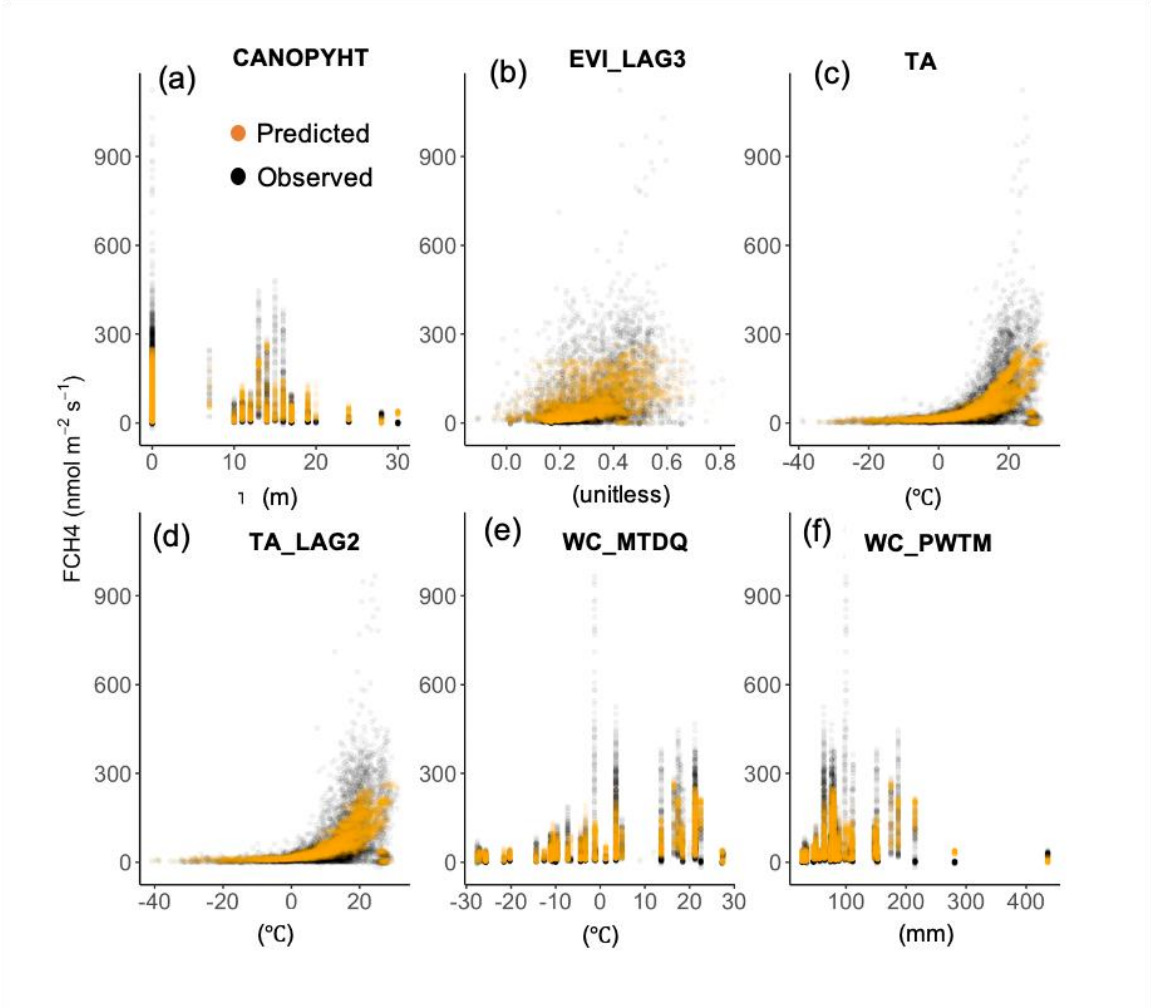

Figure S6. The functional dependency of CH_4 flux on each of the top six predictors observed in the data (black) and in model predictions (orange). The (c, d) temperature dependence appears to be exponential, while the (b) enhanced vegetation index-dependency appears to be approximately linear. The structure is more complex for the CH_4 flux dependence on (a) canopy height, and (e, f) climatological products, though CH_4 flux is highest with low canopy height ecosystems, at intermediate temperature (5-25 C) and moisture (50-200 mm y^{-1}). In

all cases, the model reproduces the mean conditions better than the highest and lowest values.

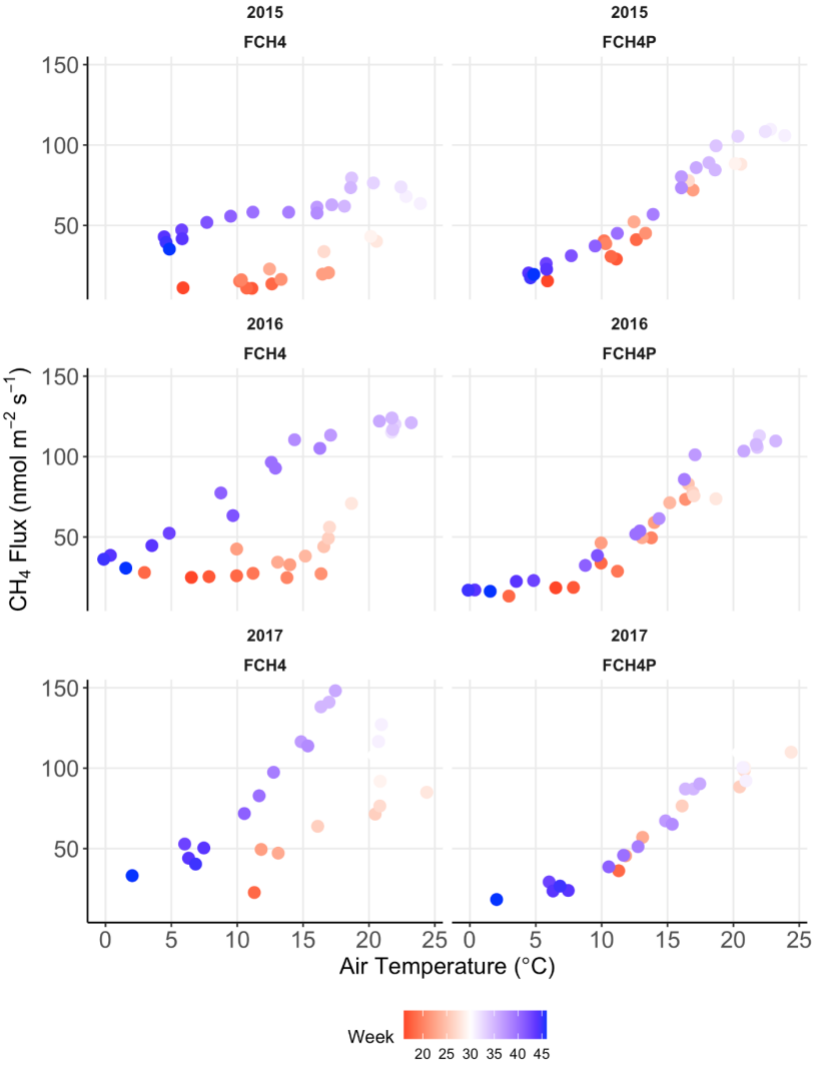

Figure S7. UpCH4 did not reproduce the hysteresis between seasonal variation in temperature and methane flux reported in (Chang et al. 2021) which was strong in the case of the site JP-BBY (shown) but varied widely in magnitude and sign across the FLUXNET-CH4 sites. The left column shows frost-free season weekly methane flux temperature dependency in the observations at the temperate bog JP-BBY and

the right column shows temperature dependency reproduced in UpCH4 that lacks the hysteresis signal.

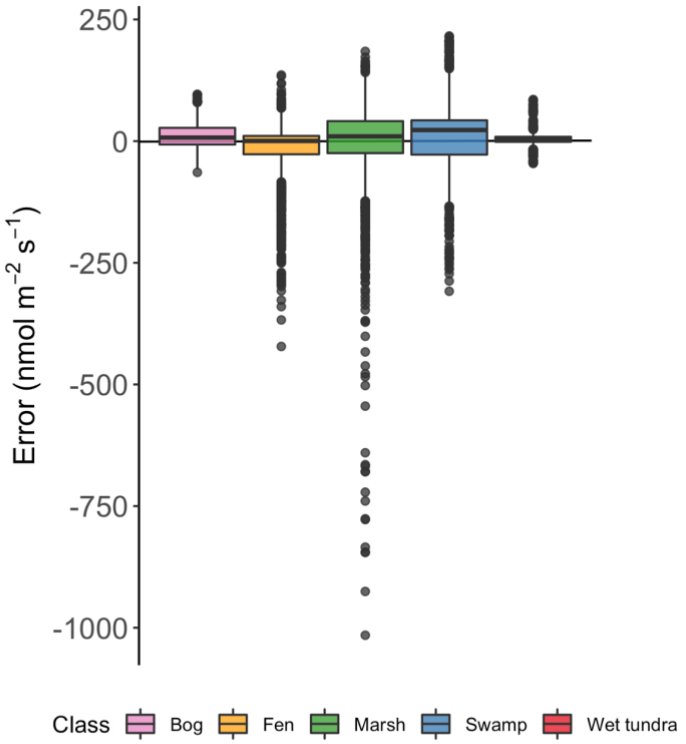

Figure S8. Model residuals (errors) computed during cross-validation grouped by wetland class. Average errors were centered around zero with dispersion that varied

by wetland class and was dominated by large negative outliers from one site (US-OWC) which exhibits exceptionally large fluxes which the model did not reproduce.

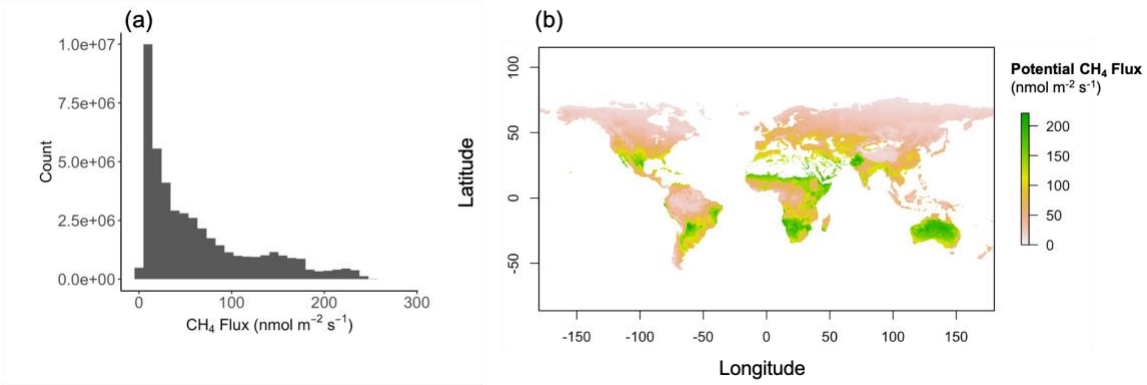

Figure S9. (a) The global time series (2001-2018) distribution of predicted freshwater wetland CH_4 fluxes and (b) map of time series mean flux, which is output during upscaling before pixel flux predictions are weighted by wetland area. Therefore, these results represent potential fluxes assuming a hypothetical full wetland cover

globally, across all regions that have non-zero wetland cover (i.e., excluding perennial desert and ice).

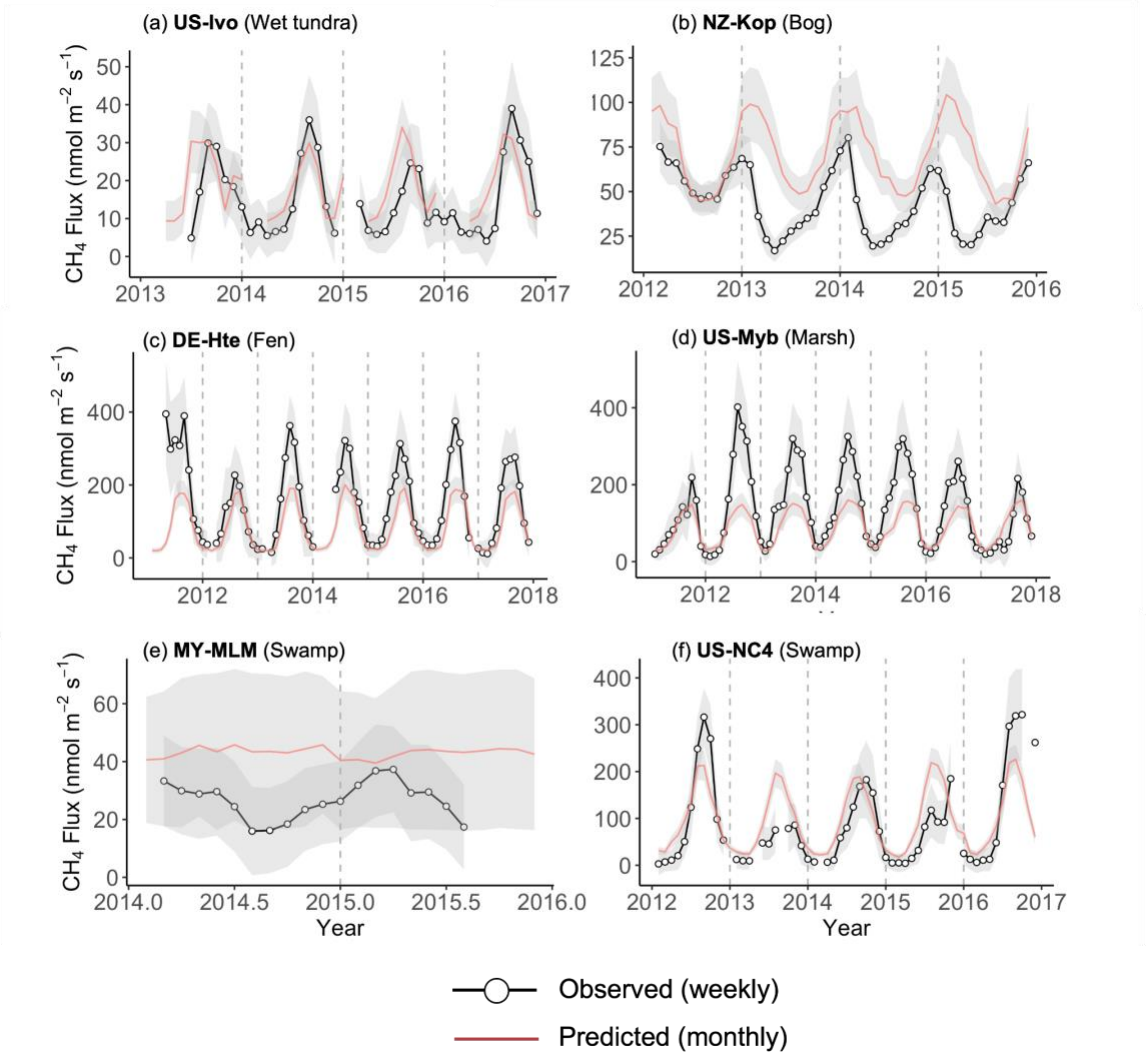

Figure S10. Six examples of gridded model performance comparing CH_4 flux predictions pixel-wise to training site fluxes. Observed weekly training fluxes (black lines and open circles) and predicted monthly fluxes (red lines) show moderate-high agreement at most sites. Note that the model predictions introduce various types of errors including (a) leading observations, (b) positive bias, (c) negative bias by underestimating the seasonal peak, (d) underestimations within the first 5 years after wetland rewetting (2011-2015; Knox et al. 2015), (e) missing seasonal cycles,

and (f) not capturing interannual variability. Grey uncertainty ribbons reflect one standard deviation around observations and predictions parameterized by CH_4 gap-filling and random uncertainties, and model ensemble dispersion, respectively. The overlapping grey ribbons in most cases provide overall confidence in model prediction when evaluated alongside uncertainties.

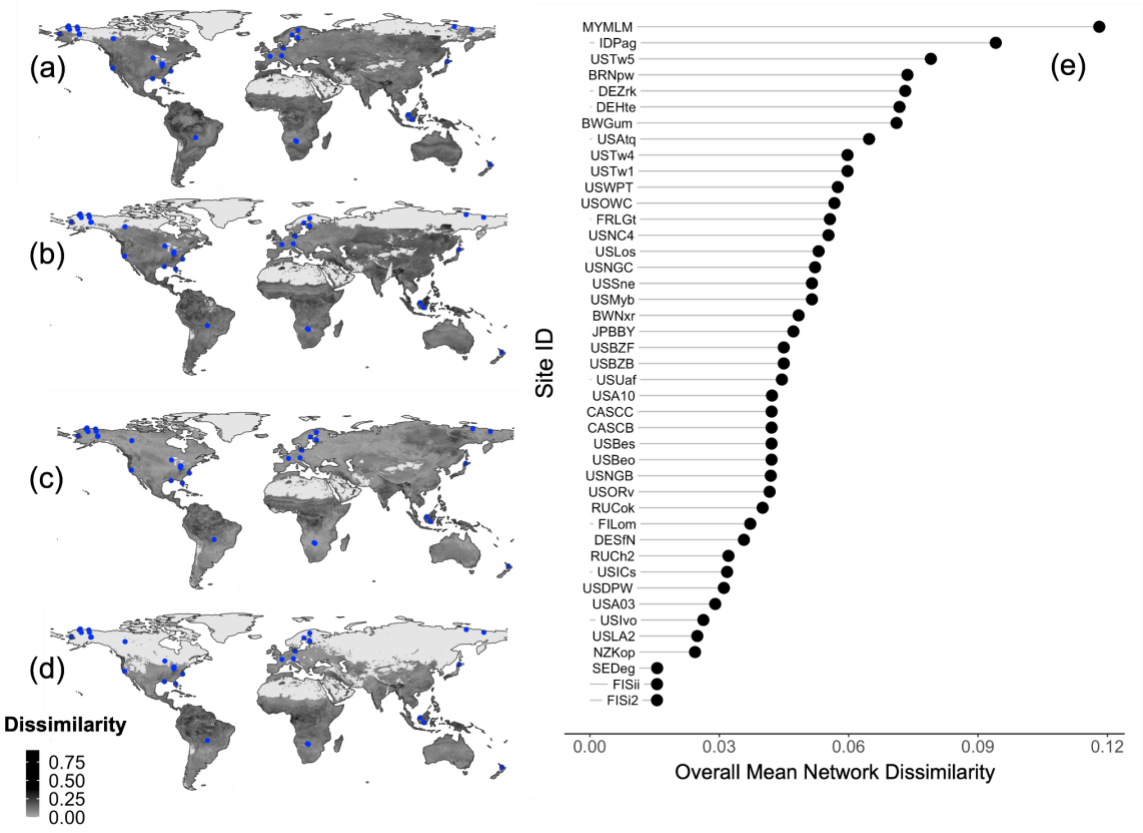

Figure S11. Global pixel-to-cluster (site) dissimilarity for (a) January, (b) April, (c) July, and (d) October, subset from the monthly 2001-2018 mean seasonal cycle. Dissimilarity was calculated as the minimum Euclidean distance between predictor conditions at a given pixel and all available site-month conditions across all tower clusters, normalized by the mean Euclidean distance between towers. Dissimilarity is relatively low (lighter shade) globally, and always is below the applicability threshold (black) of > 0.3, computed as the 95th percentile of between-tower dissimilarity. Zero-wetland cover areas from monthly WAD2M are masked out and

appear as a light grey background (e.g., Sahara Desert). Global dissimilarity is lowest in mid-to-high latitudes in July, especially in N. America and NE Eurasia, likely due to a higher density of training data in this domain and season. Year-round, tropical S. America and Africa show higher dissimilarity, likely due to sparse training data. Similarly, central and E. Asia showed elevated dissimilarity in April and October. (e) All sites are ranked by dissimilarity illustrating that most dissimilar sites are in tropical or temperate regions, with lower dissimilarity in boreal and tundra regions.

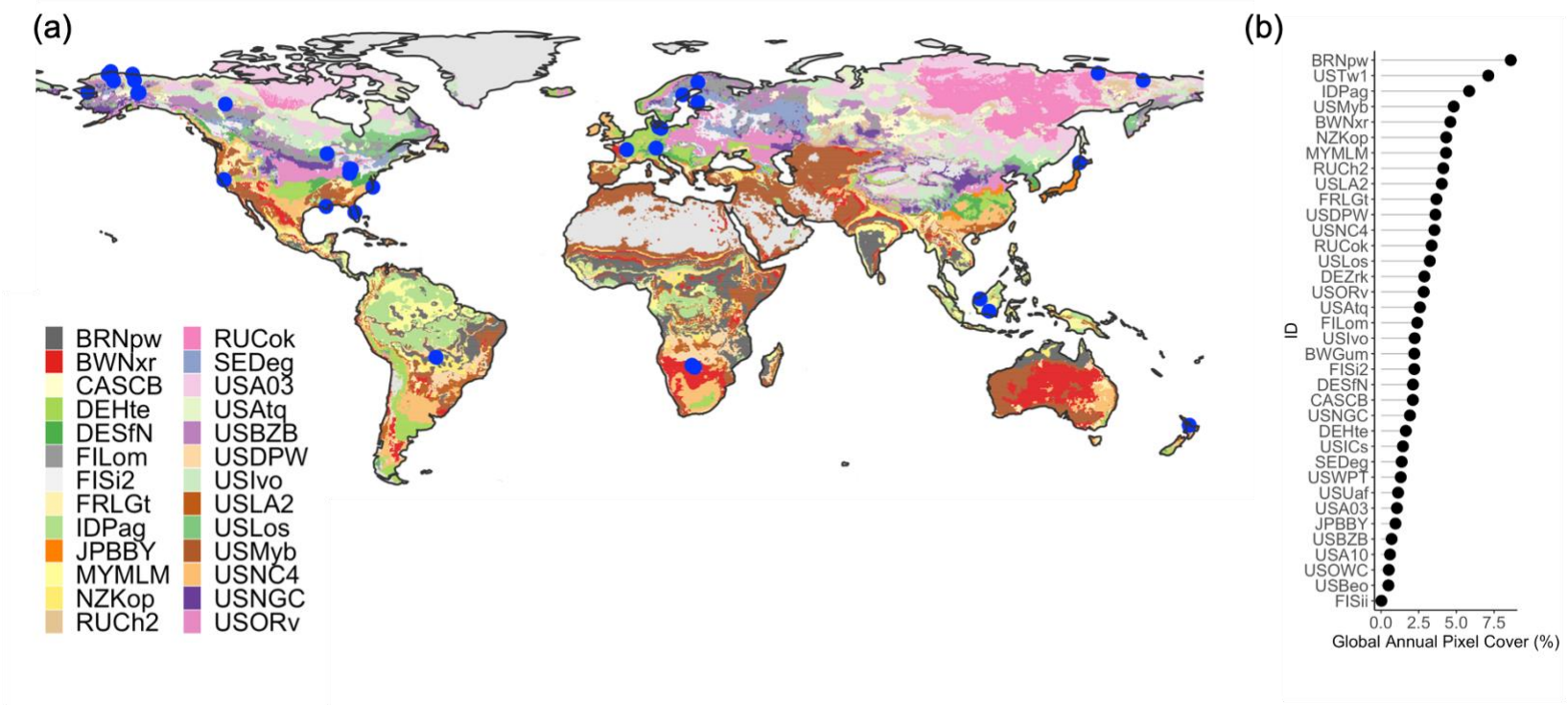

Figure S12. (a) Global distribution of tower-cluster constituencies for August of the mean seasonal cycle. August was chosen as it corresponds with the wetland area maximum, allowing for visualization of the entire terrestrial surface. (b) Constituencies are ranked by descending percent global coverage. Several of the largest constituencies are either humid tropics and semi-arid temperate or subtropical regions. Site IDs are defined in Table 2 in the manuscript.

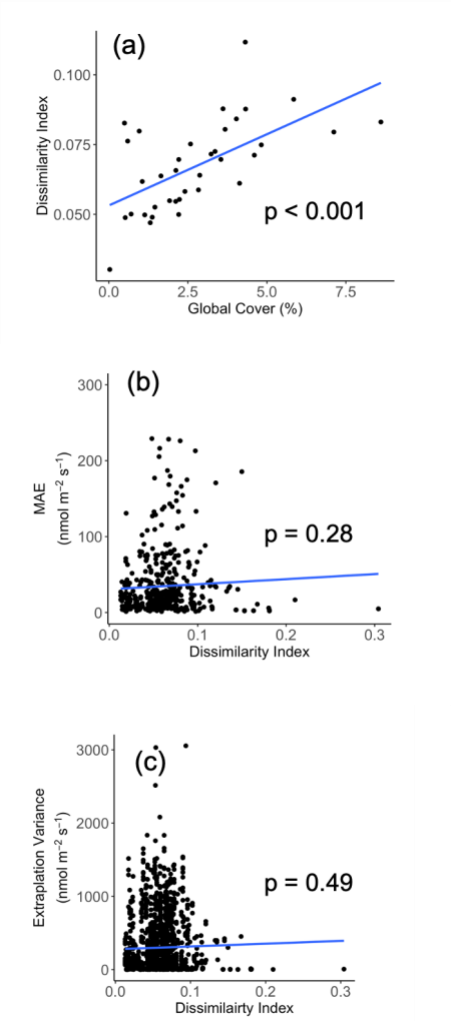

Figure S13. (a) A significant positive correlation is observed between mean dissimilarity of a constituency and its spatial extent (expressed as percentage of global ice-free land cover) reflecting lower density of towers in semi-arid and humid tropics. (b-c) No significant relationships are observed between site-month dissimilarity and the mean absolute error (MAE) or prediction variance (i.e., model uncertainty). The latter two relationships were explored as a potential means to

scale errors or uncertainties in regions of extrapolation as suggested in (Jung et al. 2020).

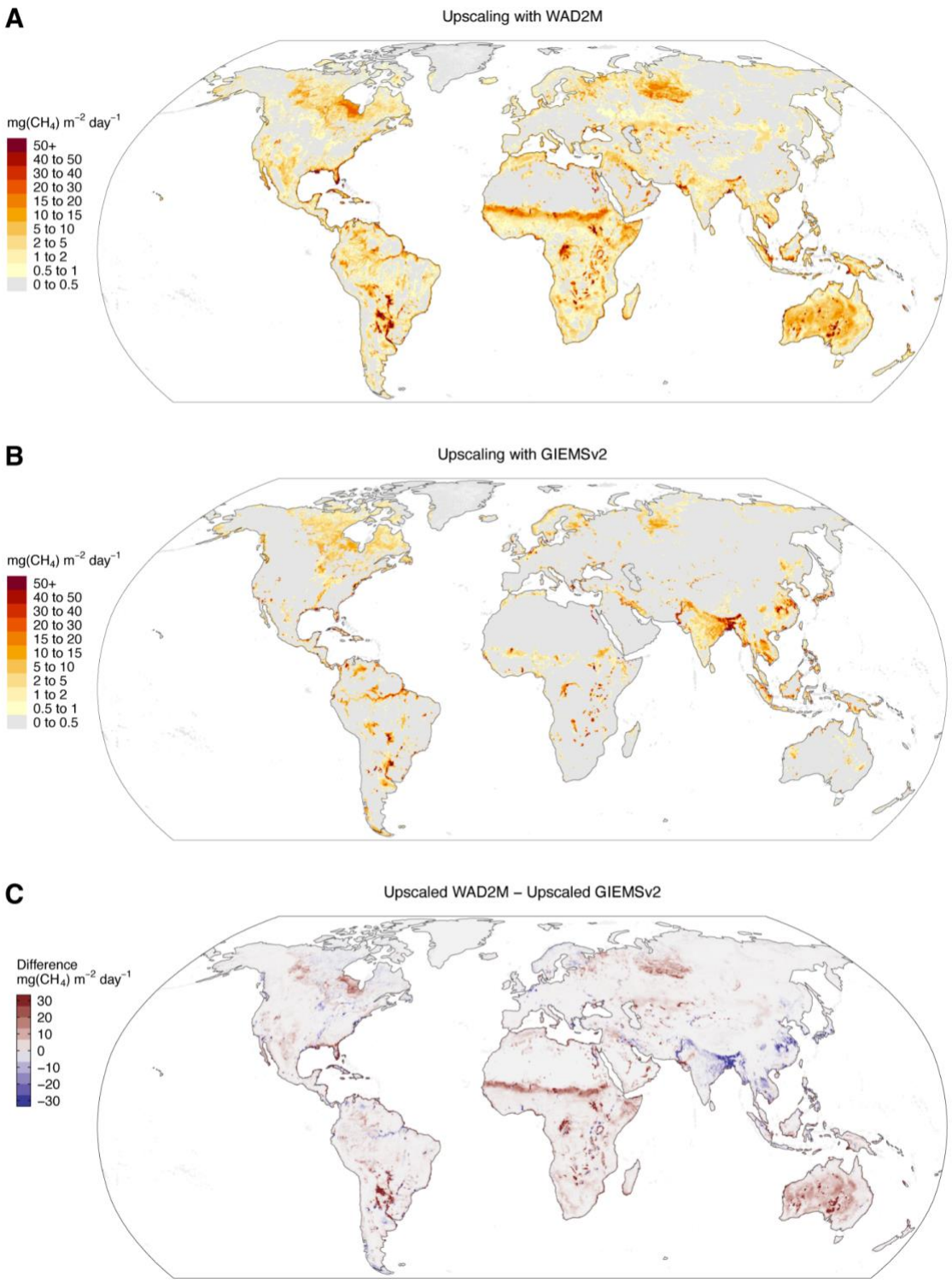
A
Upscaling with WAD2M
mg(CH4) m−2 day−1
50+
40 to 50
30 to 40
20 to 30
15 to 20
10 to 15
5 to 10
2 to 5
1 to 2
0.5 to 1
0 to 0.5
B
Upscaling with GIEMSv2
mg(CH4) m−2 day−1
50+
40 to 50
30 to 40
20 to 30
15 to 20
10 to 15
5 to 10
2 to 5
1 to 2
0.5 to 1
0 to 0.5
C
Upscaled WAD2M – Upscaled GIEMSv2
Difference
mg(CH4) m−2 day−1
30
20
10
0
−10
−20
−30

Figure S14. (a) Upscaling mean time series (2001-2018) flux using WAD2M wetland area (Zhang et al. 2021), (b) upscaling mean time series (2001-2015) flux using Global Inundation Estimate from Multiple Satellites (GIEMS-2) (Prigent et al. 2020), and (c) the difference of the two. This figure illustrates clearly how the smaller extent of GIEMS-2 corrected for only vegetated wetlands leads to lower global and regional total methane emissions than those from using WAD2M wetland area. GIEMSv2 was corrected using the same procedure as for WAD2M aside from replacing the static water cover by a monthly water cover. While most of the major wetland complexes appear in both (ex. Hudson Bay Lowlands, West Siberian Lowlands, Congo and Amazon basins) the outline of their geographic extend differs. Moreover, GIEMS-2 does not include widespread wetland coverage in Australia, the Sahel, southern Africa, or central Asia, unlike WAD2M. Wetland over Southern Asia (e.g., India and Bangladesh) and NE China are larger in GIEMS-2, a region where

extensive inundation is well documented and whose retrieval are affected by vegetation cover.

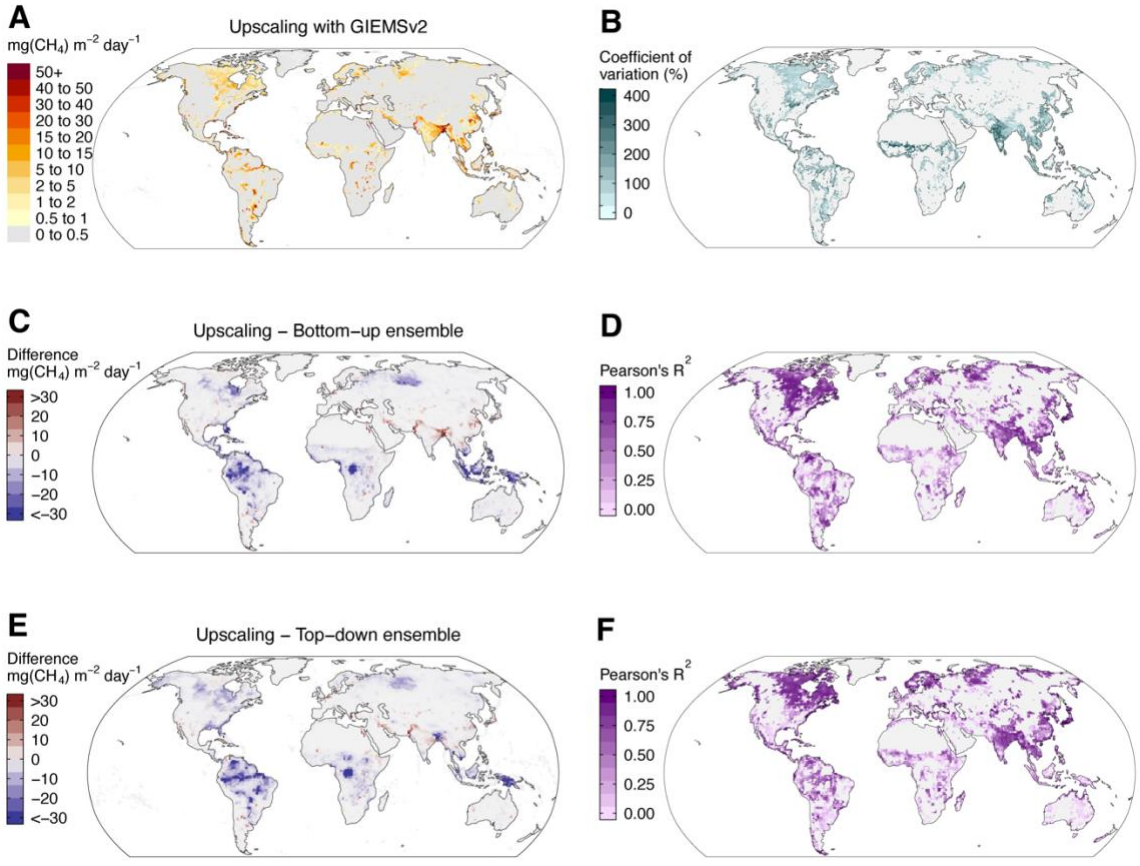

Figure S15. GIEMSv2 upscaling (A) predictions (B) uncertainties, and (C, E) differences and (D, F) seasonal cycle correlation with Global Carbon Project top-down and bottom-up ensembles.

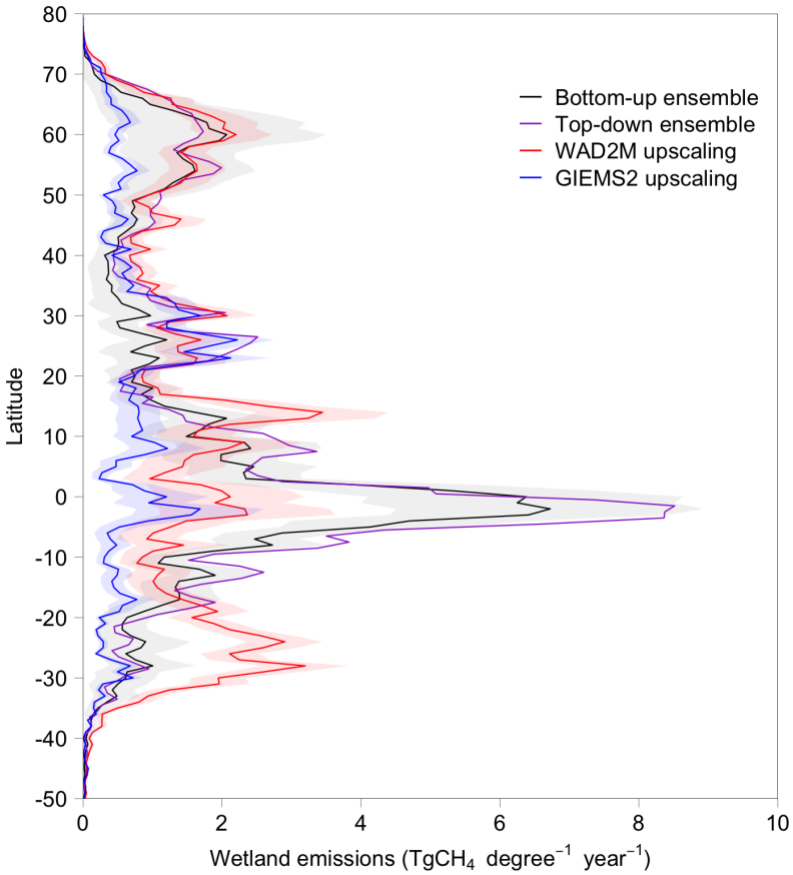

Figure S16. Total wetland emissions per 1 degree latitude across data sources. Both the WAD2M and GIEMS2 upscaling do not capture the large contribution centered at the equator. The WAD2M upscaling has higher emissions in the Southern hemisphere than all sources. Across all latitudes, WAD2M upscaling agreed best with the GCP ensemble over high Northern latitudes where the wetland cover disappearing during winter is the main methodological factor determining fluxes at those latitudes. The GIEMS2 upscaling aligns well with WetCHARTS at high Northern latitudes, although the range of the WetCHARTS ensemble (not shown) tends to suggest higher fluxes.

Supporting Tables

Table S1. (attached separately) Complete metadata table for 81 FLUXNET-CH4 Version 1.0 sites including DOI, site personnel, and whether they were considered for upscaling (Suitable for Upscaling) and used in the upscaling (Used in Upscaling). Mean annual temperature and mean annual precipitation were extracted from WorldClim 2.0 (Fick and Hijmans 2017).

Class	Count	Information Content	Example	Resolution, Frequency
Generic	1	Spatio-temporal	Potential Radiation (Peltola et al. 2019)	0.25°, 8-day
Climate	31	Spatial-only, Spatio-temporal	WorldClim 2.0 Mean Annual Temperature (Fick and Hijmans, 2017)	30 arcsec, static
Biometeorology	23	Spatio-temporal	FLUXCOM Gross Primary Productivity (Jung et al. 2020)	0.0833°, monthly
Land Cover	43	Spatial-only, Spatio-temporal	Earth Environment Land Cover (Tuanmu & Jetz, 2014)	30 arcsec, monthly
Soil & Topography	24	Spatial-only, Spatio-temporal	Geomorpho90m Elevation (Amatulli et al. 2019)	90 m, static
Greenness	18	Spatio-temporal	MODIS Enhanced Vegetation Index (Huete et al. 2002)	500 m, 8-day

Table S2. Summary, and examples, of predictors and predictor classes used in forward feature selection as part of the random forest model training.

Table S3. (attached separately) Full predictor details including DOIs for 140 unique predictors categorized into different Source Categories (modeled, tower-measured, measured, computed, remote sensing), Information Content classes (spatial or

spatiotemporal), and Classes (biometeorological, generic, climate, land cover, soil and topography, and greenness).

Predictor	Source	Timestep	Distribution	Gap-Filling	Mean Parameter	Dispersion Parameter
FCH4	Tower	Half-hourly	Laplace	Yes (ANN)	Weekly mean	Scale equal to weekly average uncertainty * 0.5 (Delwiche et al. 2021)
TA	Tower	Monthly	Normal	Yes (ERA-Interim)	Weekly mean	Standard deviation equal to 0.5 degrees Celcius (Campbell Scientific, Utah)
TA_LAG2	Tower	Monthly	Normal	Yes (ERA-Interim)	Weekly mean	Standard deviation equal to 0.5 degrees Celcius (Campbell Scientific, Utah)
wc_mtdq	Grid	Spatial	Normal	No	Extracted static value	Standard deviation equal to 0.25degree grid cell standard deviation
wc_pwtm	Grid	Spatial	Normal	No	Extracted static value	Standard deviation equal to 0.25degree grid cell standard deviation
canopyht	Grid	Spatial	Normal	No	Extracted static value	Standard deviation equal to 0.25degree grid cell standard deviation
EVI_LAG3*	Grid	8-day	Normal	Yes (with msc)	Extracted weekly value	Standard deviation equal to 0.015

*NASA Link (https://modis-land.gsfc.nasa.gov/ValStatus.php?ProductID=MOD13)

Table S4. Monte Carlo parameterization details for simulating 1,000 datasets from the original 7 variable (including CH_4 flux) model dataset selected by forward feature selection and evaluated during cross validation.

Class	Source	Predictor	Description	Temporal	Final
Biomet.	Flux Tower	TA	Air Temperature	•	•
.		TA_LAG2	Air Temperature with a two-week lag	•	•
		GPP_LEAD2	Gross Primary Production with a two-week lead	•	
		P_LEAD3	Precipitation with a three-week lead	•	
Climate	Modeled	wc_mtdq	WorldClim Mean Temperature of Driest Quarter		•
		wc_pwtm	WorldClim Precipitation of Wettest Month		•
		wc_pwtq	WorldClim Precipitation of the Wettest Quarter		
		NDSI_LAG3	MODIS Norm. Diff. Snow Index with a three-week lag	•	
Land Cover	Modeled	canopyht	Global Canopy Height		•
Greenness	Remote Sensing	EVI_LAG3	MODIS Enhanced Vegetation Index with a three-week lag	•	•
		EVI_min	Annual minimum of MODIS Enhanced Vegetation Index	•	

Table S5. Summary of the 11 predictors selected during forward feature selection including the full name, predictor class, and whether the predictor was included in the final model.

	Class	Samples	R2	NSE	nMAE	MAE	Bias
						(nmol m^{-2} s^{-1})	
All Weeks	All	6210	0.49	0.49	0.44	36.5	-1.7
Site Means	All	43	0.54	0.54	0.42	26.9	-2.6
	Bog	8	0.35	0.19	0.64	13.2	7.5
	Fen	8	0.52	0.30	0.54	25.7	-8.2
	Marsh	10	0.43	0.39	0.53	35.2	-12.0
	Swamp	6	0.06	-0.19	0.78	62.2	-13.8
	Wet tundra	11	0.02	-4.72	1.48	11.7	7.9
Mean Seasonal Cycles	All	439	0.53	0.53	0.41	31.1	-1.2
	Bog	78	0.48	0.25	0.64	16.0	7.3
	Fen	90	0.51	0.46	0.43	28.1	-7.5
	Marsh	104	0.58	0.56	0.44	41.4	-6.9
	Swamp	67	0.10	-0.03	0.77	69.1	-3.1
	Wet tundra	100	0.20	-0.40	0.74	9.4	5.1
Anomalies	All	1472	0.00	-5.11	37.2	1.25	100.0
	Bog	265	0.00	-7.42	19.9	2.21	18.5
	Fen	408	0.00	-4.53	34.8	1.34	34.6
	Marsh	421	0.00	-5.41	57.1	1.30	23.4
	Swamp	133	0.01	-4.29	66.8	1.72	14.8
	Wet tundra	245	0.00	-16.51	9.4	2.75	8.7

Table S6. A full summary of cross validation performance metrics (coefficient of determination (R^2), Nash-Sutcliffe Efficiency (NSE), mean absolute error (MAE) and normalize MAE (nMAE), and bias) for all data (weeks), and for the site mean, mean

seasonal cycles, and monthly anomalies from the mean seasonal cycle. Metrics are computed across all data within each component and grouped by wetland class.